

Z' signals in polarised top-antitop final states

L. Basso¹, K. Mimasu² and S. Moretti^{2,3}

¹*Physikalisches Institut, Albert-Ludwigs-Universität Freiburg
D-79104 Freiburg, Germany*

²*School of Physics & Astronomy, University of Southampton,
Highfield, Southampton, SO17 1BJ, UK*

³*Particle Physics Department
Rutherford Appleton Laboratory
Chilton, Didcot, Oxon OX11 0QX, UK*

Abstract

We study the sensitivity of top-antitop samples produced at all energy stages of the Large Hadron Collider (LHC) to the nature of an underlying Z' boson, in presence of full tree level standard model (SM) background effects and relative interferences. We concentrate on differential mass spectra as well as both spatial and spin asymmetries thereby demonstrating that exploiting combinations of these observables will enable one to distinguish between sequential Z' 's and those pertaining to Left-Right symmetric models as well as E_6 inspired ones, assuming realistic final state reconstruction efficiencies and error estimates.

1 Introduction

A common feature of $U(1)$ gauge extensions of the SM are Z' bosons. They appear for example in Little Higgs models [1], in theories with extra spatial dimensions [2] as well as Grand Unified Theories (GUTs) such as $SO(10)$ [3] (including Left-Right symmetric models) and E_6 [4]. Further, in some Supersymmetry (SUSY) breaking scenarios [5] and in Hidden Valley models [6], they can appear as messengers between the SM and the hidden sectors corresponding to such scenarios.

Such Z' states are best searched for at hadron colliders through a di-lepton signature in the neutral Drell-Yan (DY) process, i.e., $pp(\bar{p}) \rightarrow (\gamma, Z, Z') \rightarrow \ell^+ \ell^-$, where $\ell = e, \mu$. In fact,

the most stringent limits on Z' 's at both Tevatron and the LHC come from this signature. The Tevatron (after all its runs) places limits on the Z' mass, $M_{Z'}$, at around 1 TeV (for a sequential Z') [7] while the LHC (after the 7 TeV run) sets about 1.94 TeV (for the same Z') [8]¹. Since such an experimental signature is clean and theoretical uncertainties for inclusive quantities are well under control, see, e.g., [9], including those associated to higher order effects, both (two-loop) QCD [10] and (one-loop) EW [11] ones, one can conceive accessing the couplings of a discovered Z' (thereby providing a window on its high scale genesis) by studying the ensuing di-lepton observables (such as the leptonic invariant mass, angular distributions or spatial/spin asymmetries). Several phenomenological studies on how to measure Z' properties and couplings to SM particles in the DY channel have been performed, see [12] for general studies and [13, 14] for (rather recent) studies dedicated to specific models.

Another decay channel of Z' bosons carries phenomenological importance, despite being of less scope than the DY one in ‘discovering’ such states, i.e., $pp(\bar{p}) \rightarrow (\gamma, Z, Z') \rightarrow t\bar{t}$, into top-antitop quark pairs. Its reduced importance for Z' searches with respect to the DY case is due to the much larger background (which includes QCD production in top-antitop quark pairs), the more involved final state yielding six or more objects in the detector including jets and the associated poor efficiency in reconstructing the two heavy quarks. However, owing to the fact that the top (anti)quark decays before hadronising (so that its spin properties are effectively transmitted to the decay products) and the electromagnetic charge of the top can be tagged (via a lepton and/or a b -jet) [15], $t\bar{t}$ samples can also be useful in profiling the Z' , as the aforementioned spatial/spin asymmetries (particularly effective to pin down the couplings of the new gauge boson) can be defined in this case too [16]. Further, the large (anti)top mass induces non-trivial space/spin effects, which are not present in the DY case and are also sensitive to the nature of the intervening Z' state. Experimental collaborations at both Tevatron [17] and LHC [18] have in fact been pursuing this, in part driven by some anomalies emerged in the forward-backward asymmetry of $t\bar{t}$ samples at the Tevatron [19]. Finally, just like in the case of DY, also for $t\bar{t}$ production higher-order effects from both QCD [20] (see also [21]) and EW [22] (see also [23]) interactions are well known, including the case of polarised (anti)tops.

The purpose of this paper is to study the sensitivity of the LHC (at all its planned energy stages) to the presence of a Z' boson as well as to assess the machine ability to profile a Z' boson mediating $t\bar{t}$ production, in both standard kinematic variables as well as spatial/spin asymmetries, by adopting some benchmark scenarios for several realisations of the recalled sequential, Left-Right symmetric and E_6 based Z' models (specifically, the same as those in [14]). The plan of the paper is as follows. In the next section we describe our calculation and define the observables to be studied. In sect. 3 we report and comment on our results. Sect. 4 finally presents our conclusions.

¹A sequential Z' is a state with generic mass and same coupling to the SM particles as the Z boson. Limits in the aforementioned models are normally obtained by rescaling the results for a sequential Z' , though this implicitly assumes that the Z' cannot decay into additional extra matters present in the model spectrum.

2 Calculation

The code exploited for our study is based on helicity amplitudes, defined through the HELAS subroutines [24], and built up by means of MadGraph [25]. Initial state quarks have been taken as massless while for the (anti)top state we have taken $m_t = 175$ GeV as mass. The latter has been kept on-shell. The Parton Distribution Functions (PDFs) used were CTEQ6L1 [26], with factorisation/renormalisation scale set to $Q = \mu = 2m_t$. VEGAS [27] was used for the multi-dimensional numerical integrations.

The rest of this section introduces the asymmetry variables considered in this study of Z' models in $t\bar{t}$ final states. We will eventually explore the effect of these observables aiming to define the most suitable ones for model discrimination purposes. We will define such quantities over the entire invariant mass spectrum of the $t\bar{t}$ system, though we will exploit these in differential form as well, i.e., as a function of $M_{t\bar{t}}$.

2.1 Spatial asymmetries

Charge or spatial asymmetry in collider physics is a measure of the symmetry of the angular dependence of the matrix element for the production of a two body final state. At a hadron collider, for example, defining a polar angle, θ , as the angle between a final state particle and one of the incoming partons in the Centre-of-Mass (CM) frame, variables that are function of this angle can be constructed to probe the asymmetry of the distribution of said angle. Such an asymmetry can only be generated from a charge asymmetric initial state such as $q\bar{q}$, as opposed to, for example, the gg initial state. In QCD, the asymmetry for the $t\bar{t}$ final state is generated dominantly at Next-to-Leading Order (NLO) via interference of leading order $q\bar{q} \rightarrow t\bar{t}$ with the corresponding box diagram as well as by the interference between initial and final state gluon radiation [28]. This will also have a comparable contribution from Electro-Weak (EW) processes, both at tree- and loop-level.

2.1.1 Tevatron

Although not relevant for this paper (namely because no Z' boson has been observed at the Tevatron), we introduce here the charge asymmetry studied at the Tevatron, mostly for clarity and completeness.

The Tevatron, being a $p\bar{p}$ collider, is an ideal place to measure spatial asymmetries since the polar angle in the collider frame can more or less be identified with that of the CM frame modulo PDF effects. Statistically, both incoming partons will be valence quarks and an absolute preferred direction can be unambiguously defined. The forward-backward asymmetry A_{FB} , a possible measure of the aforementioned charge asymmetry, can then simply be defined by an integrated quantity as

$$A_{FB} = \frac{N_{t(\bar{t})}(y > 0) - N_{t(\bar{t})}(y < 0)}{N_{t(\bar{t})}(y > 0) + N_{t(\bar{t})}(y < 0)}, \quad (1)$$

where y is the rapidity of the observed top (anti)quark and $N_{t(\bar{t})}$ denotes the number of top(antitop) quarks observed in the forward ($y > 0$) or backward ($y < 0$) direction. For

this observable, the SM prediction is of order 5%, and, interestingly, both the CDF and DØ collaborations report a deviation [19]².

2.1.2 LHC

The definition of a charge asymmetry at the LHC becomes somewhat more involved. First, the charge-symmetric di-gluon initial state dominates for a significant amount of the invariant mass range for $t\bar{t}$ final states, until the parton luminosities for $q\bar{q}$ become dominant, matching that of gg at around $1 \div 2$ TeV (depending on collider energy), and remaining significant from there on. This large zero contribution dilutes the predicted SM asymmetry down to $\sim 1\%$. Secondly, even when diagrams with initial state quarks become important, the fact that the pp initial state is C -invariant necessitates the redefinition of the measured quantity itself. In this case, no preferred direction can be defined because the incoming quark will generally be a valence quark, while the antiquark must come from the sea. However, one can exploit the fact that the incoming quark will statistically carry a larger momentum fraction than the antiquark, resulting in a correlation between the boost of the $t\bar{t}$ frame and the direction of the incoming quark. Thus, defining the polar angle as, e.g., the angle between the incoming quark and the outgoing top quark, one expects a broadening of the top rapidity distribution with respect to the antitop one. The asymmetry can then be measured by restricting the rapidity range over which the top quarks are selected [30], constructing the so-called “central” (C) and “forward” (F) asymmetries:

$$A_C = \frac{N_t(|y| < y_{cut}^C) - N_{\bar{t}}(|y| < y_{cut}^C)}{N_t(|y| < y_{cut}^C) + N_{\bar{t}}(|y| < y_{cut}^C)}, \quad (2)$$

$$A_F = \frac{N_t(|y| > y_{cut}^F) - N_{\bar{t}}(|y| > y_{cut}^F)}{N_t(|y| > y_{cut}^F) + N_{\bar{t}}(|y| > y_{cut}^F)}. \quad (3)$$

Here, a rapidity cut, $y_{cut}^{C(F)}$, is chosen and the number of tops (N_t) and of antitops ($N_{\bar{t}}$) in that region are compared. Taking $y_{cut}^{C(F)} \rightarrow \infty(0)$, for $A_C(A_F)$, respectively (i.e., integrating them over the whole rapidity range), will restore $A_{C(F)} = 0$. In this analysis, $y_{cut}^C = y_{cut}^F = 0.5$.

Alternatively, one can construct variables that are function of the absolute rapidity difference of the top and antitop quarks, $\Delta y = |y_t - y_{\bar{t}}|$, which is sensitive to the CM polar angle and independent of the $t\bar{t}$ frame boost. We implemented this in two ways depending on asymmetry-enhancing kinematical cuts proposed in [31], acting on the rapidity or on the momentum along the beam axis (e.g., the z one) of the top-antitop pair, $y_{t\bar{t}} = \frac{1}{2}(y_t + y_{\bar{t}})$ and $p_{t\bar{t}}^z = p_t^z + p_{\bar{t}}^z$, referred to as “rapidity dependent” (RFB) and “one-sided” (OFB) forward-backward asymmetries, respectively:

$$A_{RFB} = \frac{N(\Delta y > 0) - N(\Delta y < 0)}{N(\Delta y > 0) + N(\Delta y < 0)} \bigg|_{|y_{t\bar{t}}| > |y_{t\bar{t}}^{cut}|}, \quad (4)$$

²It is not the aim of this paper to address such a discrepancy, since models based on colorless bosons are virtually ruled out as a possible explanation [29].

$$A_{OFB} = \frac{N(\Delta y > 0) - N(\Delta y < 0)}{N(\Delta y > 0) + N(\Delta y < 0)} \bigg|_{|p_{t\bar{t}}^z| > p_{cut}^z} . \quad (5)$$

Such kinematical cuts are designed to enhance the contributions from the $q\bar{q}$ initial state by probing regions of high partonic momentum fraction, x , where the parton luminosity of interest is more important.

2.2 Spin asymmetries

Since the top decays before it hadronises, the helicity information is preserved in its decay channels. Two relevant spin asymmetries, one double (LL) and one single (L), can then be defined as follows:

$$A_{LL} = \frac{N(+, +) + N(-, -) - N(+, -) - N(-, +)}{N_{Total}} ; \quad (6)$$

$$A_L = \frac{N(-, -) + N(-, +) - N(+, +) - N(+, -)}{N_{Total}} . \quad (7)$$

Here N denotes the number of observed events and its first(second) argument corresponds to the helicity of the top (anti)quark. Notice that such spin asymmetries can be equally defined at both the Tevatron and LHC, as they only pertain to the final state. As previously stated, such quantities can only be measured experimentally for a leptonic or top quark final state.

Defining our generic neutral current interaction in terms of gauge, vector and axial couplings g' , g_V and g_A with the Feynman rule

$$i \frac{g'}{2} \gamma^\mu (g_V - g_A \gamma^5), \quad (8)$$

the dependence on the chiral couplings of the spin asymmetries can be expressed analytically, using helicity formulas from Ref. [32] (also derived independently with the guidance of [33]):

$$A_{LL}^i \propto \left(3(g_A^t)^2 \beta^2 + (g_V^t)^2 (2 + \beta^2) \right) \left((g_V^i)^2 + (g_A^i)^2 \right), \quad (9)$$

$$A_L^i \propto g_A^t g_V^t \beta \left((g_V^i)^2 + (g_A^i)^2 \right), \quad (10)$$

for a neutral gauge boson exchanged in the s -channel. Here, i labels the initial state partons, $\beta = \sqrt{1 - 4m_t^2/\hat{s}}$ (\hat{s} being the partonic CM energy of the process) and the angular dependence has been integrated over. These imply that A_{LL} depends only on the square of the couplings similarly to the total cross section and that A_L is only non-vanishing for non-zero vector and axial couplings of the final state tops.

2.3 Benchmark models

The present analysis employs some of the benchmark models of table 1 in Ref. [14], from the $E(6)$, G_{LR} and G_{SM} parameterisations. While a brief overview is presented here, we refer the reader to the original publication for further details.

In the $E(6)$ case, a Z' boson naturally arises from the $E_6 \rightarrow SU(5) \times U(1)_\psi \times U(1)_\chi$ pattern of symmetry breaking, where it is expected that a certain linear combination of the two $U(1)$ factors, parametrized by a mixing angle θ , survives down to the TeV scale: $U(1)' = \cos \theta U(1)_\chi + \sin \theta U(1)_\psi$ (applying similarly to the symmetry generator Q_{E_6}). The coupling to fermion reads $g' Q_{E_6} Z'$, where $g' = 0.462$.

The generalised Left-Right (GLR) model originates from a left-right symmetric model, in which a TeV scale Z' boson arises, related to the following pattern of symmetry breaking: $U(1)_R \times U(1)_{B-L} \rightarrow U(1)_Y$. While in the original model only a specific combination of $U(1)_R$ and $U(1)_{B-L}$ survives, the generalised version allows a generic linear combination: $U(1)' = \cos \phi U(1)_R + \sin \phi U(1)_{B-L}$ (applying similarly to the symmetry generator Q_{GLR}). The coupling to fermions reads as $g' Q_{GLR} Z'$, where $g' = 0.595$.

The generalised sequential SM (GSM) is a class of models the includes the traditional sequential Z' boson, or Z'_{SM} , a heavier copy of the SM- Z boson. Such a boson has identical couplings to the SM- Z , with $Q_Z = Q_{T_L^3} - s_W^2 Q$, s_W^2 being the sine of the weak angle and Q the electric charge generator, respectively. Similarly to the GLR class, the GSM class is defined as a generalisation of the Z coupling mixing, such that $Q_{GSM} = \cos \alpha Q_{T_L^3} + \sin \alpha Q$, so that the Z' coupling to fermions is $g' Q_{GSM} Z'$, where $g' = 0.76$.

The benchmark models that are relevant for the present paper are collected in table 1, with the coupling to quarks split in vector and axial parts. Universal couplings between generations are assumed.

The table shows that the $E_6(G_{LR}(BL))$ models share a general feature of the Z' having a purely axial(vector) coupling to up-type quarks. Generating a tree-level charge asymmetry requires both non-zero vector and axial couplings, since the asymmetric term in the matrix element ($\propto \cos \theta$) is proportional to $g_V^i g_A^i g_V^t g_A^t$ (i being the initial state fermion and t the top quark), where the $g_{V,A}$'s are defined in section 2.3. Hence, charge asymmetry can only be generated via interference with the γ, Z background and is therefore expected to be very small for these models. Similarly for the spin asymmetries, eqs (9)–(10) imply that the E_6 -type models will only have a non-vanishing A_{LL} (at the Z' boson peak), that could serve as an extra handle to pin down parameters for these models, while A_L is, again, generated only via interference.

The rest of the models have generic, non-zero vector and axial couplings which will generate charge asymmetry, A_{LL} and A_L . As mentioned in section 2.2, A_L has the extra handle of distinguishing relative sign between the vector and axial couplings. Looking at the table, one would therefore expect the G_{LR} and G_{SM} subclasses to therefore have opposite signs providing a clear distinguishing feature.

For these reasons, we will subdivide our analysis into that of the ‘ E_6 ’ type models which will also include $G_{LR}(BL)$ and ‘Generalised’ models comprising of the rest.

$U(1)'$	Parameter	g_V^u	g_A^u	g_V^d	g_A^d
E_6 ($g' = 0.462$)	θ				
$U(1)_\chi$	0	0	-0.316	-0.632	0.316
$U(1)_\psi$	0.5π	0	0.408	0	0.408
$U(1)_\eta$	-0.29π	0	-0.516	-0.387	-0.129
$U(1)_S$	0.129π	0	-0.129	-0.581	0.452
$U(1)_N$	0.42π	0	0.316	-0.158	0.474
G_{LR} ($g' = 0.595$)	ϕ				
$U(1)_R$	0	0.5	-0.5	-0.5	0.5
$U(1)_{B-L}$	0.5π	0.333	0	0.333	0
$U(1)_{LR}$	-0.128π	0.329	-0.46	-0.591	0.46
$U(1)_Y$	0.25π	0.589	-0.354	-0.118	0.354
G_{SM} ($g' = 0.760$)	α				
$U(1)_{SM}$	-0.072π	0.193	0.5	-0.347	-0.5
$U(1)_{T_{3L}}$	0	0.5	0.5	-0.5	-0.5
$U(1)_Q$	0.5π	1.333	0	-0.666	0

Table 1: Benchmark model parameters and couplings. The angles θ , ϕ , α are defined in the text [14].

3 Results

We present here a selection of results profiling the spatial and spin asymmetry distributions of the benchmark Z' models, that were summarised in the previous section. The variables described in section 2 were computed as a function of the $t\bar{t}$ invariant mass within $\Delta M_{t\bar{t}} = |M_{Z'} - M_{t\bar{t}}| < 500$ GeV and compared to the tree-level SM predictions³. Z' boson masses of 1.7 and 2.0 TeV were taken and simulated for the LHC at 7, 8 and 14 TeV. Only results for 8 and 14 TeV CM energy are presented. However, the former energy can still be taken as representative for the 7 TeV run, as the corresponding results are very similar.

To be able to quantitatively address the distinguishability among the various models and the SM background, the statistical error of the predictions was calculated for some specific integrated luminosities. Given that an asymmetry is defined in terms of the number of events measured in some generic ‘forward’ (N_F) and ‘backward’ (N_B) directions (this is also true for spin asymmetries), the statistical error is evaluated by propagating the Poisson error on each measured quantity (i.e., $\delta N_{F(B)} = \sqrt{N_{F(B)}}$). Per given integrated luminosity \mathcal{L} , the measured number of events will be $N = \varepsilon \mathcal{L} \sigma$, σ being the cross section, yielding an uncertainty on the asymmetry A of

$$\delta A \equiv \delta \left(\frac{N_F - N_B}{N_F + N_B} \right) = \sqrt{\frac{2}{\mathcal{L} \varepsilon} \left(\frac{\sigma_F^2 + \sigma_B^2}{\sigma_{Total}^3} \right)}. \quad (11)$$

³t has also been shown that the fraction of $q\bar{q}$ initiated events could be equally enhanced by other kinematical cuts, such as on the transverse momentum of each top quark [34] as well as on the $t\bar{t}$ system [35, 36]. However, notice that the latter is not applicable to tree level studies.

Here, ε corresponds to an assumed 10% reconstruction efficiency of the $t\bar{t}$ system, considering all possible decay $t\bar{t}$ decay channels [37]. The continuous curves on the following plots are the central values for the given asymmetry, with a statistical error quantified by binning the cross sections in $M_{t\bar{t}}$ for a bin width of 50 GeV compatible with typical experimental resolutions in this quantity. We also show a selection of two bin plots integrating the cross sections over an ‘on-peak’ range ($\Delta M_{t\bar{t}} < 100$ GeV) and evaluating the corresponding partially integrated asymmetry. Finally the totally integrated asymmetries are summarised in the corresponding tables, for both the $M_{t\bar{t}}$ window cuts. Invariant mass distributions of the total cross sections for $t\bar{t}$ production are also included for reference, with the statistical error normalised by the bin width.

Although in this work we only estimate statistical uncertainties, systematics may be important as well [34, 36]. However, although the mass window selection is expected to milden their actual contribution, their inclusion would require detailed detector simulations which are beyond the scope of this paper. In this respect, it should further be noted that, by the time the LHC will reach the 14 TeV stage, where our most interesting results are applicable, systematics will be much better understood than at present.

Furthermore, the statistical significance of the measures (based on the assumption that they are independent) is calculated as follows:

$$s \equiv \frac{|A(1) - A(2)|}{\sqrt{\delta A(1)^2 + \delta A(2)^2}}. \quad (12)$$

We will make use of eq. (12) to establish the disentanglement power of the LHC for $\sqrt{s} = 14$ TeV with 100 fb^{-1} . Finally, given that the statistical error of eq. (11) has a naive $1/\sqrt{\mathcal{L}}$ dependance, it is clear that the significance of a measure, as for eq. (12), increases with luminosity. Inverting eq. (12) and solving for \mathcal{L} , we also determine the required luminosity to distinguish the models with respect to the irreducible SM background and among themselves, defining disentanglement by $s \geq 3$.

In the following, we will first present and comment on the differential distributions for the most significant asymmetries in each class, i.e. A_{LL} for the E_6 -type models and A_{LL} , A_L and A_{RFB} for the generalised models. The comparison among the two classes (and between elements in them) is done at the end, evaluating the significance of the presented distributions.

3.1 E_6 -type models

Figure 1 presents the invariant mass distributions around the Z' peak for all models with $M_{Z'} = 1.7$ TeV at both 14 and 8 TeV. These plots show that the various Z' bosons would certainly be visible in this channel, especially in the high energy and high luminosity scenario. Figure 3 profiles A_{LL} in invariant mass for the LHC at 14 TeV and Table 2 summarises integrated values for these models at both 14 and 8 TeV. When calculating statistical uncertainties, an integrated luminosity of 100 and 15 fb^{-1} is assumed for the two energies, respectively.

The analytic expression in eq. (9) shows that the observable depends on the top couplings in a similar way to the total cross section. This is reflected in the deviations from the SM

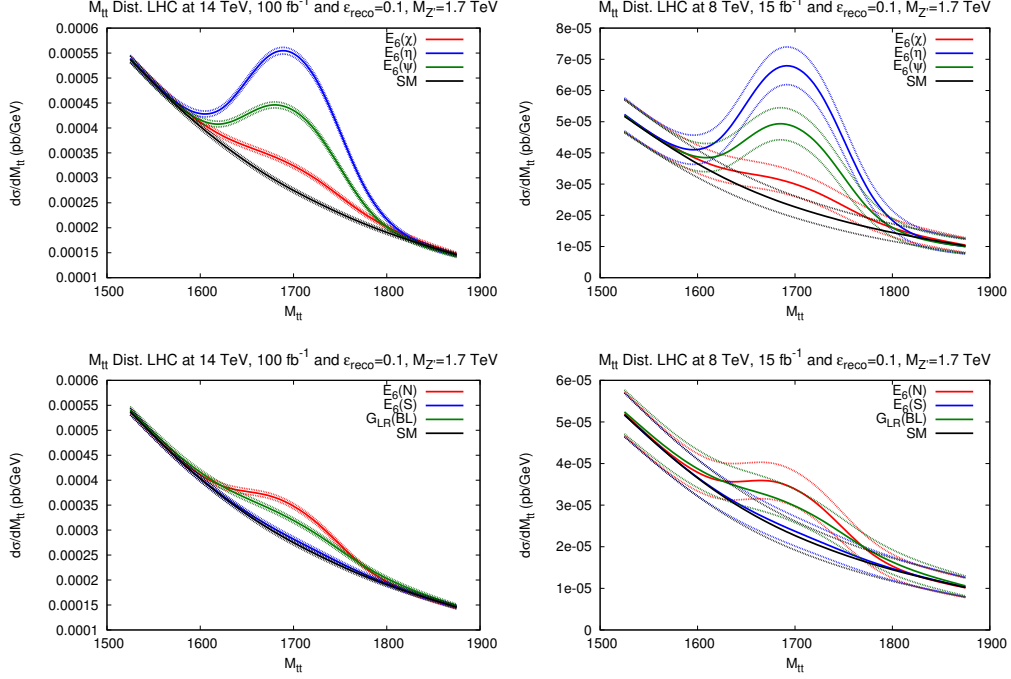


Figure 1: Invariant mass distributions for E_6 -type models for $M_{Z'}=1.7$ TeV for the LHC at 14(8) TeV and 100(15) fb^{-1} of integrated luminosity.

shown in the figures, with large effects occurring on peak whose significances increase when restricting $\Delta M_{t\bar{t}}$ as shown in Table 2. This more or less parallels the effects seen in the invariant mass distributions. In the limit of $\hat{s} \gg 4m_t^2$, A_{LL} depends identically on the vector and axial couplings of the tops and therefore cannot distinguish between the purely vector and purely axial cases of $G_{LR}(B-L)$ and E_6 models. Furthermore, Unlike A_L , it is insensitive to the relative sign between the couplings. These features are reflected by the overlapping of the $G_{LR}(B-L)$ and $E_6(\chi)$ cases, that differ in having purely vector and axial couplings respectively of different sign but of a similar magnitude. Such cases are never distinguishable neither with total cross section nor A_{LL} measurements.

Aside from these limitations, Figure 3 shows clear distinguishability of models from the SM and between one another based on differences in couplings for the high energy case except when the up type coupling is too small, as for $E_6(S)$. (Table 1 implies that this model would be much better suited to the $b\bar{b}$ channel.) Table 2 further improves on these numbers by comparing integrated values focused around the Z' peak which gives scope for sensitivity to deviations from the SM and limited distinguishability even at low energy.

3.2 Generalised models

In contrast to the E_6 -type models, the generalised models have non-zero vector and axial couplings to all quarks. Therefore, all of the asymmetry observables can be generated at tree-level on peak. Combined with their consequently higher cross sections, shown in the

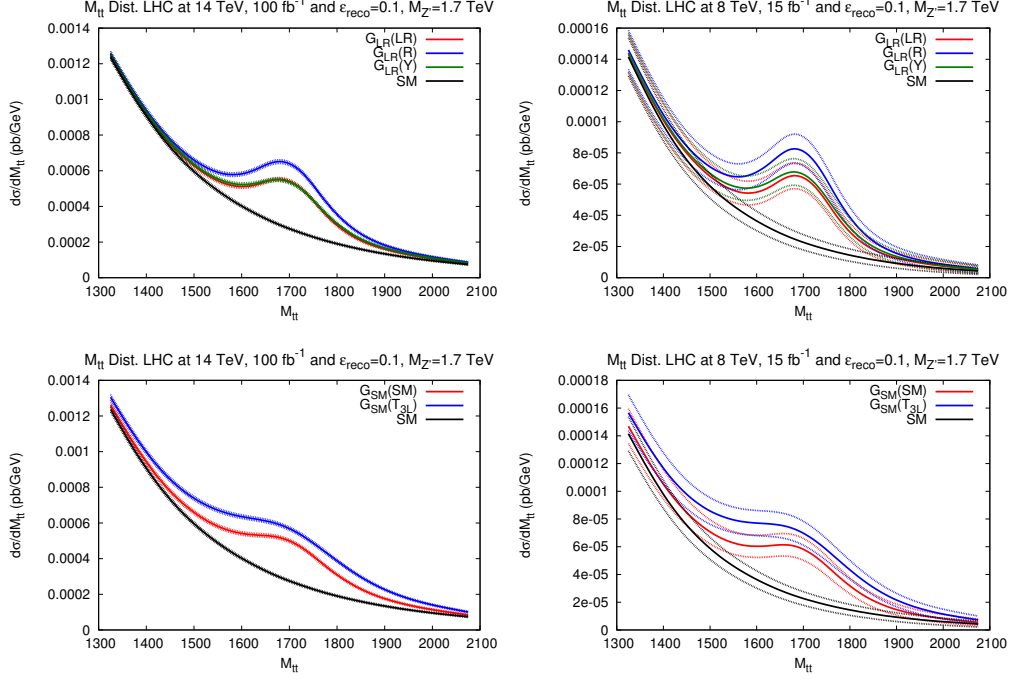


Figure 2: Invariant mass distributions for generalised models with $M_{Z'}=1.7$ TeV for the LHC at 14(8) TeV and 100(15) fb^{-1} of integrated luminosity.

invariant mass distributions of Figure 2, this set of models has clear signatures at the LHC even at 8 TeV. Figures 4 and 5 and Tables 3 and 4 profile the spin asymmetry variables A_{LL} and A_L , showing large deviations from the SM case. As already noted, the difference in sign in the A_L contributions of the G_{LR} and G_{SM} models allows for the best distinguishing power over all the models investigated. This is particularly important for the specific case of the $G_{LR}(LR/Y)$ and $G_{SM}(SM)$ models that do not appear distinguishable in the invariant mass distributions nor in the other variables, but do so in the A_L two-bin plots.

The spatial asymmetry variables are also clearly visible in these models and since they all are very similar kinematically, we show plots for the variable with the best discrimination power⁴ only (as we will see in the next section), i.e., A_{RFB} , in Figure 6 in differential form while its integrated values are found in Table 5.

3.3 Significance and luminosity analysis

Tables 8 to 10 summarise the significance measures between various models as defined in eq. (12) for A_{LL} , A_L and A_{RFB} , for the entries in Tables 2 to 5, respectively.

Generally speaking, A_L provides the best overall discrimination power, when the variable is non-vanishing at the Z' peak. Beside preserving the relative sign between the top quark chiral couplings, allowing to distinguish the G_{SM} from the G_{LR} class, it also has the highest

⁴This is expected from the fact that the variable incorporates a kinematical cut to enhance the $q\bar{q}$ contribution as discussed in section 2.1

significance when comparing the Z' models in these classes with the SM expectation and among themselves. For the E_6 -type cases, where A_L is too small to be measured, the other spin variable A_{LL} comes into play. We observe that its significance is always bigger than the spatial asymmetries, A_{RFB} being the biggest amongst the latter. As mentioned, this variable can be used to distinguish all the presented models from the SM background. Regarding the disentanglement among models, we observe that the narrower mass window and lower Z' mass always perform better, although noting that 1.7 TeV is bordering on being ruled out already in other searches. Models with very large width, such as the G_{SM} ones, deliver a bigger significance in the larger invariant mass cut. Finally, The significance of these asymmetry measures is finally evaluated for the case of both E_6 and generalised models in Tables 8–10, for A_{LL} , A_L and A_{RFB} .

From all these tables it is clear that some models can be distinguished in early stages of the LHC at $\sqrt{s} = 14$ TeV, i.e., with less than 100 fb^{-1} . At the same time, the question of what is the required luminosity to discriminate among models also quantify how powerful a variable is. Tables 6 and 7 address the distinguishability of the various models using the spin and spatial asymmetries with increasing integrated luminosity. These reinforce the fact that the models can generally be separated using these observables for reasonable integrated luminosities when the sizes (and signs) of the relevant couplings differ enough. The spin asymmetries provide the best distinctions and A_{RFB} performs the best among the spatial asymmetries.

Although certain models remain unresolvable even with full luminosity, 300 fb^{-1} , $\mathcal{O}(1) \text{ fb}^{-1}$ of integrated luminosity is already enough to disentangle the generalised models using A_L . With A_{LL} , E_6 -type models start being distinguishable with $\mathcal{O}(10) \text{ fb}^{-1}$. $\mathcal{O}(50) \text{ fb}^{-1}$ is required for full discrimination with A_{LL} , as well as to have confirmations for the generalised models with the spatial asymmetries, among which A_{RFB} outperforms all the others requiring less integrated luminosity.

4 Conclusions

Z' 's appears in many BSM scenarios and are under intense scrutiny presently at the LHC owing to a clear leptonic signature they offer through the DY process. However, in order to profile this new object (i.e., measuring not only its mass and width but also its couplings to all matter, its spin, its CP quantum numbers, etc.), a combination between the DY results and those obtained in other channels may be necessary. Channels where asymmetries in the event distribution can be defined are particularly powerful, as such observables are very sensitive to the chiral structure of the Z' -fermion-antifermion vertices involved and to the spin nature of the new particle. Hence, amongst these, the $t\bar{t}$ decay channel of a Z' boson is particularly relevant and accessible at the LHC, albeit less clean and efficient than the DY ones.

We have therefore presented a phenomenological study of classes of Z' models in both spin and spatial asymmetries of $t\bar{t}$ production. A selection of observables has been defined and profiled as a function of the $t\bar{t}$ invariant mass showing that there is much scope to observe deviations from the SM and even distinguish between various models, particularly for spin

asymmetries, using a narrow invariant mass range around the Z' peak. Further, we quantified distinguishability between models and considered the significance of such differences with respect to the integrated luminosity.

It is worth noting that, as stated in Section 1, the classes of models studied are a set of benchmarks put forward for experimentalists to set bounds on Z' masses which are best probed in the di-lepton channels. Other models featuring heavy neutral gauge bosons would be even better suited to the $t\bar{t}$ channel, such as leptophobic/top-phillic Z' 's occurring in composite/multi-site and extra-dimensional models [38, 39]. The profiling techniques discussed in this study would be increasingly more applicable in these top-friendly scenarios. Furthermore, it has been assumed that all other exotic matter states decoupled for simplicity while they may have non-negligible effects on widths and branching ratios that should be considered when moving away from model independent methods [39].

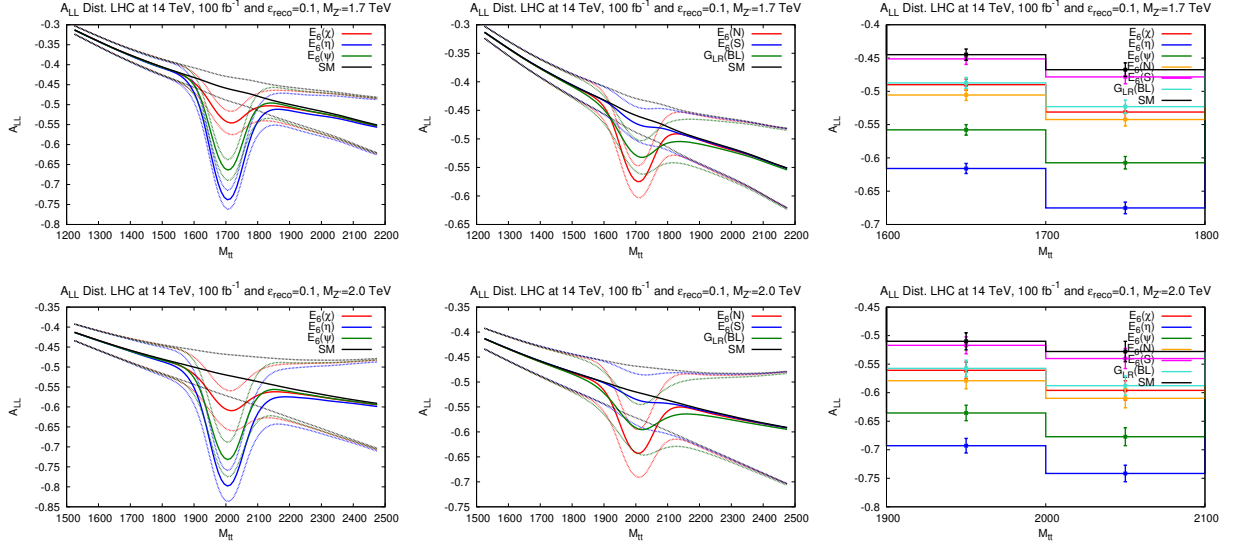


Figure 3: A_{LL} binned in $M_{t\bar{t}}$ for E_6 -type models with $M_{Z'}=1.7$ (upper) and 2 (lower) TeV for the LHC at 14 TeV assuming 100 fb^{-1} of integrated luminosity. Rightmost plots show the distribution in two 100 GeV bins either side of the Z' peak. Dotted lines and error bars represent statistical uncertainty calculated as described in the text.

$A_{LL}(\times 10)$	$\sqrt{s} = 14 \text{ TeV}$	$\mathcal{L}_{int} = 100 \text{ fb}^{-1}$	$\sqrt{s} = 8 \text{ TeV}$	$\mathcal{L}_{int} = 15 \text{ fb}^{-1}$
$M_{Z'} = 1.7 \text{ TeV}$	$\Delta M_{t\bar{t}} < 0.5 \text{ TeV}$	$\Delta M_{t\bar{t}} < 0.1 \text{ TeV}$	$\Delta M_{t\bar{t}} < 0.5 \text{ TeV}$	$\Delta M_{t\bar{t}} < 0.1 \text{ TeV}$
SM	-3.79 ± 0.05	-4.54 ± 0.07	-4.75 ± 0.39	-5.65 ± 0.61
$E_6(\chi)$	-3.88 ± 0.05	-5.07 ± 0.06	-4.85 ± 0.39	-6.35 ± 0.58
$E_6(\eta)$	-4.17 ± 0.05	-6.42 ± 0.06	-5.22 ± 0.38	-7.85 ± 0.48
$E_6(\psi)$	-4.01 ± 0.05	-5.79 ± 0.06	-5.02 ± 0.33	-7.22 ± 0.52
$E_6(N)$	-3.90 ± 0.05	-5.21 ± 0.06	-4.88 ± 0.39	-6.54 ± 0.57
$E_6(S)$	-3.80 ± 0.05	-4.62 ± 0.07	-4.76 ± 0.39	-5.76 ± 0.61
$G_{LR}(B-L)$	-3.88 ± 0.05	-5.02 ± 0.06	-4.86 ± 0.39	-6.31 ± 0.57
$M_{Z'} = 2.0 \text{ TeV}$	$\Delta M_{t\bar{t}} < 0.5 \text{ TeV}$	$\Delta M_{t\bar{t}} < 0.1 \text{ TeV}$	$\Delta M_{t\bar{t}} < 0.5 \text{ TeV}$	$\Delta M_{t\bar{t}} < 0.1 \text{ TeV}$
SM	-4.66 ± 0.09	-5.17 ± 0.11	-5.68 ± 0.84	-6.32 ± 1.23
$E_6(\chi)$	-4.77 ± 0.09	-5.76 ± 0.11	-5.81 ± 0.83	-7.03 ± 1.14
$E_6(\eta)$	-5.13 ± 0.09	-7.15 ± 0.10	-6.26 ± 0.80	-8.44 ± 0.89
$E_6(\psi)$	-4.94 ± 0.09	-6.54 ± 0.10	-6.02 ± 0.82	-7.90 ± 1.00
$E_6(N)$	-4.79 ± 0.09	-5.92 ± 0.11	-5.84 ± 0.83	-7.23 ± 1.11
$E_6(S)$	-4.67 ± 0.09	-5.27 ± 0.11	-5.70 ± 0.84	-6.43 ± 1.22
$G_{LR}(B-L)$	-4.77 ± 0.09	-5.70 ± 0.11	-5.82 ± 0.83	-7.00 ± 1.13

Table 2: Summary of integrated A_{LL} values around the Z' peak for E_6 -type models with $M_{Z'}=1.7$ and 2 TeV at the LHC at 14 and 8 TeV assuming 100 and 15 fb^{-1} of integrated luminosity respectively.

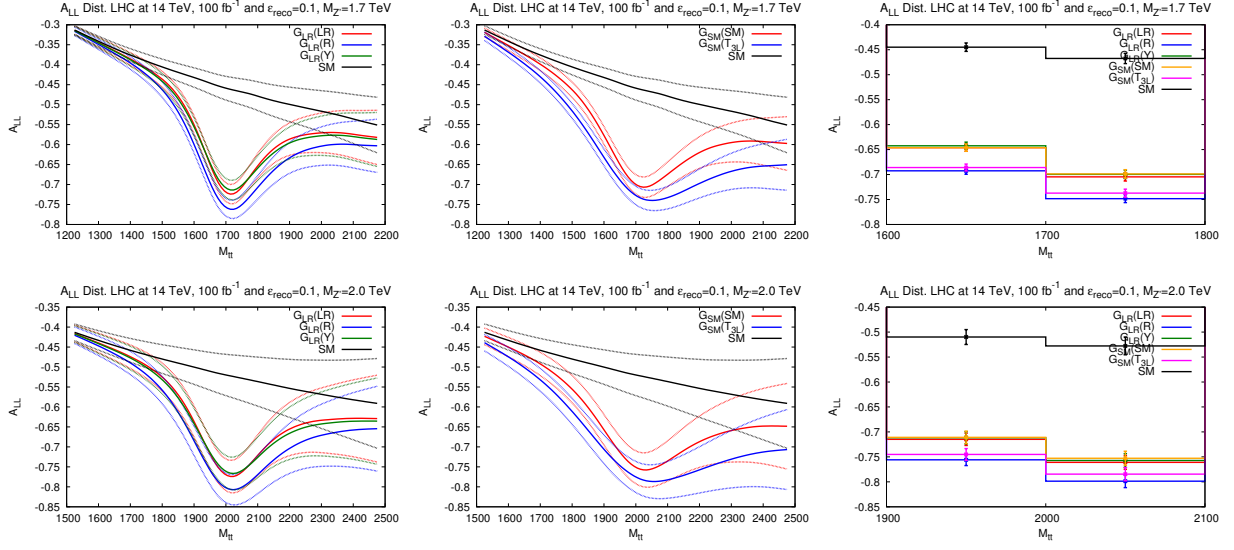


Figure 4: A_{LL} distributions binned in $M_{t\bar{t}}$ for generalised models with $M_{Z'}=1.7$ (*upper*) and 2 (*lower*) TeV for the LHC at 14 TeV assuming 100 fb^{-1} of integrated luminosity. Rightmost plots show the distribution in two 100 GeV bins either side of the Z' peak. Dotted lines and error bars represent statistical uncertainty calculated as described in the text.

$A_{LL}(\times 10)$	$\sqrt{s} = 14 \text{ TeV}$	$\mathcal{L}_{int} = 100 \text{ fb}^{-1}$	$\sqrt{s} = 8 \text{ TeV}$	$\mathcal{L}_{int} = 15 \text{ fb}^{-1}$
$M_{Z'} = 1.7 \text{ TeV}$	$\Delta M_{t\bar{t}} < 0.5 \text{ TeV}$	$\Delta M_{t\bar{t}} < 0.1 \text{ TeV}$	$\Delta M_{t\bar{t}} < 0.5 \text{ TeV}$	$\Delta M_{t\bar{t}} < 0.1 \text{ TeV}$
SM	-3.79 ± 0.05	-4.54 ± 0.07	-4.75 ± 0.39	-5.65 ± 0.61
$G_{LR}(LR)$	-4.41 ± 0.05	-6.72 ± 0.06	-5.48 ± 0.37	-8.03 ± 0.45
$G_{LR}(R)$	-4.70 ± 0.05	-7.18 ± 0.05	-5.83 ± 0.36	-8.38 ± 0.41
$G_{LR}(Y)$	-4.43 ± 0.05	-6.68 ± 0.05	-5.55 ± 0.37	-8.02 ± 0.44
$G_{SM}(SM)$	-4.52 ± 0.05	-6.69 ± 0.06	-5.64 ± 0.37	-8.04 ± 0.45
$G_{SM}(T_{3L})$	-4.94 ± 0.04	-7.09 ± 0.05	-6.12 ± 0.35	-8.31 ± 0.41
$M_{Z'} = 2.0 \text{ TeV}$	$\Delta M_{t\bar{t}} < 0.5 \text{ TeV}$	$\Delta M_{t\bar{t}} < 0.1 \text{ TeV}$	$\Delta M_{t\bar{t}} < 0.5 \text{ TeV}$	$\Delta M_{t\bar{t}} < 0.1 \text{ TeV}$
SM	-4.66 ± 0.09	-5.17 ± 0.11	-5.68 ± 0.84	-6.32 ± 1.23
$G_{LR}(LR)$	-5.41 ± 0.08	-7.36 ± 0.09	-6.53 ± 0.78	-8.51 ± 0.85
$G_{LR}(R)$	-5.74 ± 0.08	-7.75 ± 0.09	-6.90 ± 0.75	-8.79 ± 0.76
$G_{LR}(Y)$	-5.44 ± 0.08	-7.32 ± 0.09	-6.62 ± 0.77	-8.53 ± 0.82
$G_{SM}(SM)$	-5.53 ± 0.08	-7.30 ± 0.09	-6.69 ± 0.77	-8.51 ± 0.86
$G_{SM}(T_{3L})$	-5.99 ± 0.08	-7.63 ± 0.09	-7.16 ± 0.72	-8.72 ± 0.78

Table 3: Summary of integrated A_{LL} values around the Z' peak for the generalised models with $M_{Z'}=1.7$ and 2 TeV at the LHC at 14 and 8 TeV assuming 100 and 15 fb^{-1} of integrated luminosity respectively.

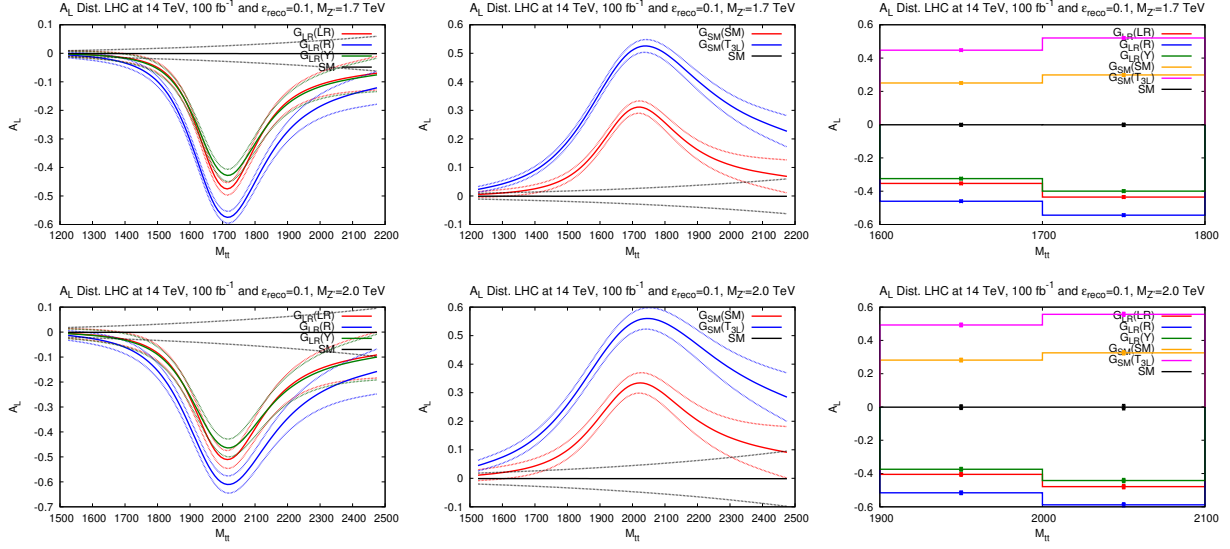


Figure 5: A_L binned in $M_{t\bar{t}}$ for generalised models with $M_{Z'}=1.7$ (*upper*) and 2 (*lower*) TeV for the LHC at 14 TeV assuming 100 fb^{-1} of integrated luminosity. Rightmost plots show the distribution in two 100 GeV bins either side of the Z' peak. Dotted lines and error bars represent statistical uncertainty calculated as described in the text.

$A_L(\times 10)$	$\sqrt{s} = 14 \text{ TeV}$	$\mathcal{L}_{int} = 100 \text{ fb}^{-1}$	$\sqrt{s} = 8 \text{ TeV}$	$\mathcal{L}_{int} = 15 \text{ fb}^{-1}$
$M_{Z'} = 1.7 \text{ TeV}$	$\Delta M_{t\bar{t}} < 0.5 \text{ TeV}$	$\Delta M_{t\bar{t}} < 0.1 \text{ TeV}$	$\Delta M_{t\bar{t}} < 0.5 \text{ TeV}$	$\Delta M_{t\bar{t}} < 0.1 \text{ TeV}$
SM	-0.009 ± 0.044	-0.010 ± 0.059	-0.017 ± 0.35	-0.020 ± 0.53
$G_{LR}(LR)$	-0.971 ± 0.042	-3.90 ± 0.05	-1.37 ± 0.33	-5.36 ± 0.40
$G_{LR}(R)$	-1.51 ± 0.04	-4.98 ± 0.05	-2.14 ± 0.32	-6.53 ± 0.37
$G_{LR}(Y)$	-0.938 ± 0.042	-3.58 ± 0.05	-1.40 ± 0.33	-5.05 ± 0.38
$G_{SM}(SM)$	0.802 ± 0.042	2.71 ± 0.05	1.16 ± 0.32	3.79 ± 0.38
$G_{SM}(T_{3L})$	1.90 ± 0.04	4.80 ± 0.05	2.70 ± 0.31	6.36 ± 0.38
$M_{Z'} = 2.0 \text{ TeV}$	$\Delta M_{t\bar{t}} < 0.5 \text{ TeV}$	$\Delta M_{t\bar{t}} < 0.1 \text{ TeV}$	$\Delta M_{t\bar{t}} < 0.5 \text{ TeV}$	$\Delta M_{t\bar{t}} < 0.1 \text{ TeV}$
SM	-0.011 ± 0.088	-0.012 ± 0.10	-0.020 ± 0.73	-0.020 ± 1.04
$G_{LR}(LR)$	-1.38 ± 0.07	-4.38 ± 0.08	-1.91 ± 0.66	-5.81 ± 0.75
$G_{LR}(R)$	-2.09 ± 0.07	-5.49 ± 0.08	-2.91 ± 0.64	-6.97 ± 0.69
$G_{LR}(Y)$	-1.34 ± 0.07	-4.05 ± 0.08	-1.99 ± 0.65	-5.54 ± 0.71
$G_{SM}(SM)$	1.12 ± 0.07	3.01 ± 0.08	1.59 ± 0.65	4.07 ± 0.71
$G_{SM}(T_{3L})$	2.55 ± 0.07	5.21 ± 0.08	3.53 ± 0.62	6.74 ± 0.71

Table 4: Summary of integrated A_L values around the Z' peak for the generalised models with $M_{Z'}=1.7$ and 2 TeV at the LHC at 14 and 8 TeV assuming 100 and 15 fb^{-1} of integrated luminosity respectively.

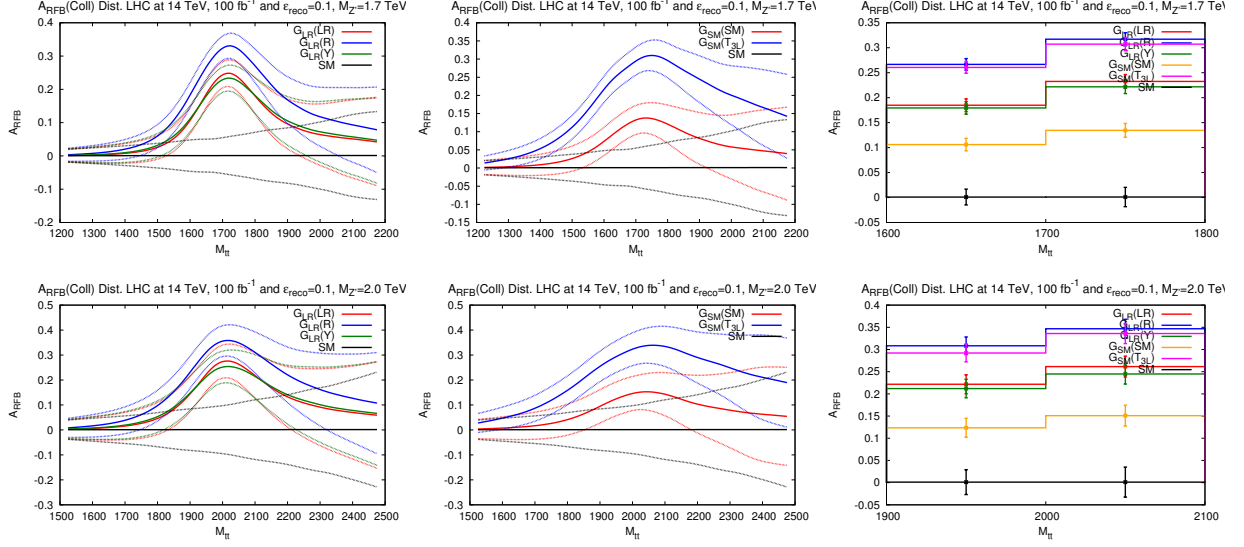


Figure 6: A_{RFB} binned in $M_{t\bar{t}}$ for generalised models with $M_{Z'}=1.7$ (upper) and 2 (lower) TeV for the LHC at 14 TeV assuming 100 fb^{-1} of integrated luminosity. Rightmost plots show the distribution in two 100 GeV bins either side of the Z' peak. Dotted lines and error bars represent statistical uncertainty calculated as described in the text.

$A_{RFB}(\times 10)$	$\sqrt{s} = 14 \text{ TeV}$	$\mathcal{L}_{int} = 100 \text{ fb}^{-1}$	$\sqrt{s} = 8 \text{ TeV}$	$\mathcal{L}_{int} = 15 \text{ fb}^{-1}$
$M_{Z'} = 1.7 \text{ TeV}$	$\Delta M_{t\bar{t}} < 0.5 \text{ TeV}$	$\Delta M_{t\bar{t}} < 0.1 \text{ TeV}$	$\Delta M_{t\bar{t}} < 0.5 \text{ TeV}$	$\Delta M_{t\bar{t}} < 0.1 \text{ TeV}$
SM	0.008 ± 0.089	0.010 ± 0.122	0.018 ± 0.819	0.02 ± 1.35
$G_{LR}(LR)$	0.501 ± 0.084	2.07 ± 0.09	0.776 ± 0.760	3.27 ± 0.88
$G_{LR}(R)$	0.873 ± 0.081	2.89 ± 0.09	1.34 ± 0.73	4.24 ± 0.79
$G_{LR}(Y)$	0.523 ± 0.083	1.99 ± 0.09	0.807 ± 0.745	2.96 ± 0.82
$G_{SM}(SM)$	0.337 ± 0.083	1.19 ± 0.09	0.524 ± 0.743	1.88 ± 0.86
$G_{SM}(T_{3L})$	1.10 ± 0.08	2.81 ± 0.09	1.71 ± 0.70	4.15 ± 0.81
$M_{Z'} = 2.0 \text{ TeV}$	$\Delta M_{t\bar{t}} < 0.5 \text{ TeV}$	$\Delta M_{t\bar{t}} < 0.1 \text{ TeV}$	$\Delta M_{t\bar{t}} < 0.5 \text{ TeV}$	$\Delta M_{t\bar{t}} < 0.1 \text{ TeV}$
SM	0.010 ± 0.167	0.011 ± 0.216	0.02 ± 1.86	0.03 ± 2.84
$G_{LR}(LR)$	0.745 ± 0.153	2.40 ± 0.16	1.13 ± 1.67	3.70 ± 1.82
$G_{LR}(R)$	1.26 ± 0.15	3.26 ± 0.14	1.90 ± 1.58	4.67 ± 1.62
$G_{LR}(Y)$	0.768 ± 0.151	2.27 ± 0.15	1.17 ± 1.62	3.30 ± 1.66
$G_{SM}(SM)$	0.495 ± 0.152	1.36 ± 0.16	0.75 ± 1.62	2.07 ± 1.73
$G_{SM}(T_{3L})$	1.54 ± 0.14	3.12 ± 0.15	2.33 ± 1.51	4.54 ± 1.67

Table 5: Summary of integrated A_{RFB} values around the Z' peak for generalised models with $M_{Z'}=1.7$ and 2 TeV at the LHC at 14 and 8 TeV assuming 100 and 15 fb^{-1} of integrated luminosity respectively.

$A_L \searrow A_{LL}$	SM	$E_6(\chi)$	$E_6(\eta)$	$E_6(\psi)$	$E_6(N)$	$E_6(S)$	$G_{LR}(B-L)$	$G_{LR}(LR)$	$G_{LR}(R)$	$G_{LR}(Y)$	$G_{SM}(SM)$	$G_{SM}(T_{3L})$
SM	–	62.6	5.1	10.6	38.7	>300	77.5	3.8	2.7	3.9	4.0	3.0
$E_6(\chi)$		–	10.2	32.7	>300	90.7	>300	7.1	4.6	7.5	7.7	5.2
$E_6(\eta)$			–	48.4	13.1	5.6	9.5	>300	45.3	>300	>300	70.7
$E_6(\psi)$				–	51.7	12.3	28.2	24.2	11.1	26.8	28.2	13.7
$E_6(N)$					–	51.6	>300	8.8	5.4	9.3	9.5	6.2
$E_6(S)$						–	117.8	4.2	3.0	4.3	4.4	3.3
$G_{LR}(B-L)$							–	6.6	4.3	6.9	7.1	4.9
$G_{LR}(LR)$	0.8							–	95.9	>300	>300	200.0
$G_{LR}(R)$	0.5							9.3	–	78.9	72.0	>300
$G_{LR}(Y)$	0.9							105.8	5.6	–	>300	151.7
$G_{SM}(SM)$	1.6							0.2	0.2	0.2	–	133.9
$G_{SM}(T_{3L})$	0.5							0.1	0.1	0.1	2.4	–

Table 6: Required integrated luminosity (in fb^{-1}) at the LHC at 14 TeV to “distinguish” Z' models from the SM background and among themselves, for (upper triangle) A_{LL} and (lower triangle) A_L , for $M_{Z'}=2.0$ TeV. Models are disentangled if $s = 3$. No value is given for A_L for the E_6 -type models because such asymmetry is too small to be observed.

Spatial	SM	$G_{LR}(LR)$	$G_{LR}(R)$	$G_{LR}(Y)$	$G_{SM}(SM)$	$G_{SM}(T_{3L})$
SM	–	11.4(14.0)	5.6(6.6)	12.2(14.8)	35.7(42.6)	6.4(7.5)
$G_{LR}(LR)$	13.2(30.9)	–	55.0(59.1)	>300(>300)	42.6(55.1)	83.5(94.0)
$G_{LR}(R)$	7.1(14.3)	61.2(118.8)	–	38.7(51.7)	11.3(13.4)	>300(>300)
$G_{LR}(Y)$	13.7(33.0)	>300(>300)	55.3(98.4)	–	52.3(63.0)	56.1(79.6)
$G_{SM}(SM)$	40.0(97.6)	40.9(122.5)	11.8(28.9)	44.4(144.5)	–	14.0(16.6)
$G_{SM}(T_{3L})$	7.8(16.7)	94.0(204.9)	>300(>300)	82.8(161.5)	14.0(37.5)	–

Table 7: Required integrated luminosity (in fb^{-1}) at the LHC at 14 TeV to “distinguish” Z' models from the SM background and among themselves, for (upper triangle) $A_{RFB}(A_{OFB})$ and (lower triangle) $A_C(A_F)$, for $M_{Z'}=2.0$ TeV. Models are disentangled if $s = 3$.

A_{LL}	SM	$E_6(\chi)$	$E_6(\eta)$	$E_6(\psi)$	$E_6(N)$	$E_6(S)$	$G_{LR}(B-L)$	$G_{LR}(LR)$	$G_{LR}(R)$	$G_{LR}(Y)$	$G_{SM}(SM)$	$G_{SM}(T_{3L})$
SM	–	5.7(1.3)	20.4(5.4)	13.6(3.1)	7.3(1.6)	0.8(0.1)	5.2(1.3)	23.6(8.8)	30.7(12.9)	24.9(9.1)	23.3(10.3)	29.6(18.0)
$E_6(\chi)$	3.8(0.9)	–	15.9(4.1)	8.5(1.8)	1.6(0.3)	4.9(1.1)	0.6($\ll 1$)	19.4(7.5)	27.0(11.6)	20.6(7.8)	19.1(9.1)	25.9(16.6)
$E_6(\eta)$	13.3(3.7)	9.4(2.8)	–	7.4(2.3)	14.3(3.8)	19.5(5.2)	16.5(4.1)	3.5(3.4)	9.7(7.5)	3.3(3.7)	3.2(4.9)	8.6(12.0)
$E_6(\psi)$	9.2(2.2)	5.2(1.3)	4.3(1.5)	–	6.8(1.6)	12.7(3.0)	9.1(1.8)	11.0(5.7)	17.8(9.8)	11.4(5.9)	10.6(7.2)	16.6(14.5)
$E_6(N)$	4.8(1.0)	1.0(0.2)	8.3(2.7)	4.2(1.2)	–	6.4(1.4)	2.2(0.3)	17.8(7.2)	25.2(11.3)	18.8(7.5)	17.4(8.8)	24.1(16.2)
$E_6(S)$	0.6(0.1)	3.1(0.8)	12.6(3.6)	8.5(2.1)	4.2(0.9)	–	4.3(1.1)	22.8(8.6)	29.8(12.7)	23.9(8.9)	22.5(10.2)	28.7(17.8)
$G_{LR}(B-L)$	3.4(0.9)	0.4($\ll 1$)	9.8(2.8)	5.7(1.3)	1.4(0.2)	2.8(0.8)	–	20.0(7.5)	27.7(11.6)	21.3(7.8)	19.7(9.1)	26.5(16.6)
$G_{LR}(LR)$	15.4(6.2)	11.3(5.3)	1.6(2.3)	6.1(3.9)	10.1(5.1)	14.7(6.1)	11.7(5.3)	–	5.9(4.1)	0.5(0.3)	0.4(1.6)	4.7(8.3)
$G_{LR}(R)$	18.2(9.0)	14.0(8.1)	4.5(5.1)	9.0(6.6)	12.9(7.9)	17.4(8.9)	14.4(8.1)	3.1(2.9)	–	7.1(3.8)	6.3(2.5)	1.3(3.7)
$G_{LR}(Y)$	15.1(6.5)	11.0(5.6)	1.3(2.6)	5.8(4.2)	9.9(5.4)	14.4(6.4)	11.4(5.6)	0.3(0.3)	3.4(2.7)	–	0.1(1.3)	5.8(8.0)
$G_{SM}(SM)$	15.0(7.2)	10.8(6.3)	1.1(3.3)	5.6(4.9)	9.7(6.1)	14.3(7.1)	11.3(6.3)	0.5(1.1)	3.5(1.9)	0.2(0.8)	–	5.1(6.6)
$G_{SM}(T_{3L})$	17.3(11.0)	13.2(10.1)	3.6(7.1)	8.1(8.7)	12.0(10.0)	16.6(11.0)	13.6(10.1)	2.1(5.1)	0.9(2.2)	2.4(4.9)	2.6(4.1)	–

Table 8: Significance for A_{LL} as in Tables 2–3, for the LHC at 14 TeV only. Upper triangle for $M_{Z'} = 1.7$ TeV and lower triangle for $M_{Z'}=2.0$ TeV. Figures refer to $\Delta M_{t\bar{t}} < 100(500)$ GeV.

A_L	SM	$G_{LR}(LR)$	$G_{LR}(R)$	$G_{LR}(Y)$	$G_{SM}(SM)$	$G_{SM}(T_{3L})$
SM	–	50.0(22.8)	63.9(37.3)	45.9(22.0)	35.0(19.2)	61.8(47.4)
$G_{LR}(LR)$	34.1(12.2)	–	15.3(9.3)	4.5(0.6)	93.5(29.9)	123.0(49.5)
$G_{LR}(R)$	42.8(18.5)	9.8(7.2)	–	19.8(9.9)	108.8(39.9)	123.0(60.3)
$G_{LR}(Y)$	31.5(11.8)	2.9(0.4)	12.7(7.6)	–	89.0(29.3)	118.5(48.9)
$G_{SM}(SM)$	23.6(10.1)	65.3(25.3)	75.1(32.4)	62.4(24.8)	–	29.5(18.9)
$G_{SM}(T_{3L})$	40.8(22.8)	84.8(39.7)	84.8(46.9)	81.8(39.3)	19.4(14.4)	–

Table 9: Significance for A_L as in Table 4, for the LHC at 14 TeV only. Upper triangle for $M_{Z'} = 1.7$ TeV and lower triangle for $M_{Z'}=2.0$ TeV. Figures refer to $\Delta M_{t\bar{t}} < 100(500)$ GeV.

A_{RFB}	SM	$G_{LR}(LR)$	$G_{LR}(R)$	$G_{LR}(Y)$	$G_{SM}(SM)$	$G_{SM}(T_{3L})$
SM	–	13.6(4.0)	19.0(7.2)	13.1(4.2)	7.8(2.7)	18.5(9.1)
$G_{LR}(LR)$	8.9(3.2)	–	6.4(3.2)	0.6(0.2)	6.9(1.4)	5.8(5.2)
$G_{LR}(R)$	12.6(5.6)	4.0(2.4)	–	7.1(3.0)	13.4(4.6)	0.6(2.0)
$G_{LR}(Y)$	8.6(3.4)	0.6(0.1)	4.8(2.3)	–	6.3(1.6)	6.4(5.0)
$G_{SM}(SM)$	5.0(2.1)	4.6(1.2)	8.9(3.6)	4.1(1.3)	–	12.7(6.6)
$G_{SM}(T_{3L})$	11.8(7.0)	3.3(3.8)	0.7(1.4)	4.0(3.7)	8.0(5.1)	–

Table 10: Significance for A_{RFB} as in Table 5, for the LHC at 14 TeV only. Upper triangle for $M_{Z'} = 1.7$ TeV and lower triangle for $M_{Z'}=2.0$ TeV. Figures refer to $\Delta M_{t\bar{t}} < 100(500)$ GeV.

Acknowledgements

The work of KM and SM is partially supported through the NExT Institute. LB is supported by the Deutsche Forschungsgemeinschaft through the Research Training Group grant GRK 1102 *Physics of Hadron Accelerators*. We would like to thank E. Alvarez for pointing out the discussion on systematic uncertainties.

References

- [1] For a review, see M. Schmaltz and D. Tucker-Smith, *Ann. Rev. Nucl. Part. Sci.* **55**, 229 (2005).
- [2] For a review, see J. L. Hewett and M. Spiropulu, *Ann. Rev. Nucl. Part. Sci.* **52**, 397 (2002).
- [3] For a review, see: R. N. Mohapatra, *Unification and Supersymmetry*, Springer, New York, 1986.
- [4] For a review, see J. L. Hewett and T. G. Rizzo, *Phys. Rept.* **183**, 193 (1989).
- [5] For a review, see D. J. H. Chung, L. L. Everett, G. L. Kane, S. F. King, J. D. Lykken and L. T. Wang, *Phys. Rept.* **407**, 1 (2005).
- [6] M. J. Strassler and K. M. Zurek, *Phys. Lett. B* **651**, 374 (2007).
- [7] CDF Collaboration, *Phys. Rev. Lett.* **102**, 091805 (2009) and *Phys. Rev. Lett.* **102**, 031801 (2009); D0 Collaboration, note 4375-Conf and note 4577-Conf.
- [8] ATLAS Collaboration, *Phys. Rev. Lett.* **107**, 272002 (2011); CMS Collaboration, *JHEP* **1105**, 093 (2011) and CMS PAS EXO-11-019.
- [9] See, e.g.: B. Fuks, M. Klasen, F. Ledroit, Q. Li and J. Morel, *Nucl. Phys. B* **797** (2008) 322

- [10] R. Hamberg, W. L. van Neerven and T. Matsuura, Nucl. Phys. B **359**, 343 (1991); [Erratum, *ibidem* **644**, 403 (2002)]; C. Anastasiou, L. J. Dixon, K. Melnikov and F. Petriello, Phys. Rev. D **69**, 094008 (2004); K. Melnikov and F. Petriello, Phys. Rev. D **74**, 114017 (2006).
- [11] U. Baur, O. Brein, W. Hollik, C. Schappacher and D. Wackerroth, Phys. Rev. D **65**, 033007 (2002).
- [12] See, e.g.: P. Langacker, R. W. Robinett and J. L. Rosner, Phys. Rev. D **30**, 1470 (1984); A. Leike, Phys. Rept. **317**, 143 (1999); T. G. Rizzo, arXiv:hep-ph/0610104; P. Langacker, arXiv:0801.1345 [hep-ph]; M. S. Carena, A. Daleo, B. A. Dobrescu and T. M. P. Tait, Phys. Rev. D **70**, 093009 (2004); M. Dittmar, A. S. Nicollrat and A. Djouadi, Phys. Lett. B **583**, 111 (2004); J. Erler, P. Langacker, S. Munir and E. Rojas, JHEP **0908**, 017 (2009).
- [13] C. Coriano, A. E. Faraggi and M. Guzzi, Phys. Rev. D **78**, 015012 (2008); and *ibidem* **53**, 421 (2008); Y. Li, F. Petriello and S. Quackenbush, Phys. Rev. D **80**, 055018 (2009); R. Diener, S. Godfrey and T. A. W. Martin, Phys. Rev. D **83**, 115008 (2011); J. Erler, P. Langacker, S. Munir and E. Rojas, JHEP **1111**, 076 (2011) F. Petriello and S. Quackenbush, Phys. Rev. D **77**, 115004 (2008); E. Accomando, S. De Curtis, D. Dominici and L. Fedeli, Phys. Rev. D **83**, 015012 (2011) and *ibidem* **79**, 055020 (2009); P. Athron, S. F. King, D. J. Miller, S. Moretti and R. Nevzorov, Phys. Rev. D **80**, 035009 (2009) and Phys. Lett. B **681**, 448 (2009); C.P. Hays, A. V. Kotwal and O. Stelzer-Chilton, Mod. Phys. Lett. A **24**, 2387 (2009); E. Salvioni, A. Strumia, G. Villadoro and F. Zwirner, JHEP **1003**, 010 (2010); E. Salvioni, G. Villadoro and F. Zwirner, JHEP **0911**, 068 (2009); P. Osland, A. A. Pankov, A. V. Tsytrinov and N. Paver, Phys. Rev. D **79**, 115021 (2009).
- [14] E. Accomando, A. Belyaev, L. Fedeli, S. F. King and C. Shepherd-Themistocleous, Phys. Rev. D **83**, 075012 (2011).
- [15] T. Stelzer and S. Willenbrock, Phys. Lett. B **374**, 169 (1996); G. Mahlon and S.J. Parke, Phys. Rev. D **D53** (1996) 4886 and *ibidem* **81**, 074024 (2010); W. Bernreuther, A. Brandenburg, Z.G. Si and P. Uwer, Phys. Rev. Lett. **87**, 242002 (2001) and hep-ph/0410197.
- [16] D. Choudhury, R. M. Godbole, S. D. Rindani and P. Saha, Phys. Rev. D **84**, 014023 (2011); R. M. Godbole, K. Rao, S. D. Rindani and R. K. Singh, JHEP **1011**, 144 (2010); B. Xiao, Y. K. Wang, Z. Q. Zhou and S. H. Zhu, Phys. Rev. D **83**, 057503 (2011) and E. L. Berger, Q. H. Cao, C. R. Chen and H. Zhang, Phys. Rev. D **83**, 114026 (2011); R. Diener, S. Godfrey and T. A. W. Martin, Phys. Rev. D **83**, 115008 (2011); R. Frederix and F. Maltoni, JHEP **0901**, 047 (2009). J. Cao, L. Wu and J. M. Yang, Phys. Rev. D **83**, 034024 (2011)
- [17] CDF Collaboration, arXiv:1107.5063 [hep-ex] and Phys. Rev. D **84**, 072003 (2011); D0 Collaboration, Phys. Lett. B **668**, 98 (2008).

- [18] ATLAS Collaboration, ATLAS-CONF-2011-087 and ATLAS-CONF-2011-123; CMS Collaboration, CMS PAS EXO-11-006 and CMS PAS EXO-11-055.
- [19] V. M. Abazov *et al.* [D0 Collaboration], Phys. Rev. D **84**, 112005 (2011).
- [20] W. Bernreuther, A. Brandenburg, Z. G. Si and P. Uwer, Int. J. Mod. Phys. A **18**, 1357 (2003); N. Kidonakis and R. Vogt, Phys. Rev. D **78**, 074005 (2008); M. Cacciari, S. Frixione, M. L. Mangano, P. Nason and G. Ridolfi, JHEP **0809**, 127 (2008); M. Czakon and A. Mitov, Nucl. Phys. B **824**, 111 (2010); K. Melnikov and M. Schulze, JHEP **0908**, 049 (2009); A. Bredenstein, A. Denner, S. Dittmaier and S. Pozzorini, JHEP **1003**, 021 (2010).
- [21] P. Nason, S. Dawson and R.K. Ellis, Nucl. Phys. B **303**, 607 (1988) and *ibidem* **327**, 49 (1989); W. Beenakker, H. Kuijf, W.L. van Neerven and J. Smith, Phys. Rev. D **40**, 54 (1989); W. Beenakker, W.L. van Neerven, R. Meng, G.A. Schuler and J. Smith, Nucl. Phys. B **351**, 507 (1991); M.L. Mangano, P. Nason and G. Ridolfi, Nucl. Phys. B **373**, 295 (1992).
- [22] S. Moretti, M. R. Nolten and D. A. Ross, Phys. Lett. B **639**, 513 (2006) [Erratum, *ibidem* **660**, 607 (2008)]; J. H. Kuhn, A. Scharf and P. Uwer, Eur. Phys. J. C **51**, 37 (2007); W. Hollik and M. Kollar, Phys. Rev. D **77**, 014008 (2008); W. Bernreuther, M. Fucker and Z. G. Si, Phys. Rev. D **78**, 017503 (2008) and Int. J. Mod. Phys. A **21**, 914 (2006).
- [23] W. Beenakker, A. Denner, W. Hollik, R. Mertig, T. Sack and D. Wackeroth, Nucl. Phys. B **411**, 343 (1994); C. Kao, G. A. Ladinsky and C. P. Yuan, Int. J. Mod. Phys. A **12**, 1341 (1997); C. Kao and D. Wackeroth, Phys. Rev. D **61**, 055009 (2000).
- [24] H. Murayama, I. Watanabe and K. Hagiwara, KEK Report 91-11, January 1992.
- [25] T. Stelzer and W. F. Long, Comput. Phys. Commun. **81**, 357 (1994).
- [26] J. Pumplin, D. R. Stump, J. Huston, H. L. Lai, P. Nadolsky and W. K. Tung, JHEP **07**, 012 (2002).
- [27] G.P. Lepage, J. Comp. Phys. **27**, 192 (1978) [Erratum, preprint CLNS-80/447, March 1980].
- [28] R. W. Brown, D. Sahdev and K. O. Mikaelian, Phys. Rev. Lett. **43**, 1069 (1979). J. H. Kuhn and G. Rodrigo, Phys. Rev. D **59**, 054017 (1999).
- [29] J. A. Aguilar-Saavedra and M. Perez-Victoria, JHEP **1109**, 097 (2011); Phys. Rev. D **84**, 115013 (2011).
- [30] O. Antunano, J. H. Kuhn and G. Rodrigo, Phys. Rev. D **77**, 014003 (2008)
- [31] Z. -q. Zhou, B. Xiao, Y. -k. Wang and S. -h. Zhu, Phys. Rev. D **83**, 094022 (2011)

- [32] M. Arai, N. Okada, K. Smolek and V. Simak, *Acta Phys. Polon. B* **40** (2009) 93
- [33] K. Hagiwara and D. Zeppenfeld, *Nucl. Phys. B* **274**, 1 (1986).
- [34] J. L. Hewett, J. Shelton, M. Spannowsky, T. M. P. Tait and M. Takeuchi, *Phys. Rev. D* **84** (2011) 054005
- [35] J. H. Kuhn and G. Rodrigo, *JHEP* **1201**, 063 (2012)
- [36] E. Alvarez, LHC using $t\bar{t}$ bar transverse momentum,”
- [37] G. L. Bayatian *et al.* [CMS Collaboration], CERN-LHCC-2006-001; “ATLAS: Detector and physics performance technical design report. Volume 1,” CERN-LHCC-99-14; “ATLAS: Detector and physics performance technical design report. Volume 2,” CERN-LHCC-99-15.
- [38] E. Accomando, I. Antoniadis and K. Benakli, *Nucl. Phys. B* **579**, 3 (2000) G. Panico and A. Wulzer, *JHEP* **1109**, 135 (2011) S. De Curtis, M. Redi and A. Tesi, arXiv:1110.1613 [hep-ph]. C. T. Hill, *Phys. Lett. B* **345**, 483 (1995)
- [39] L. Basso, K. Mimasu and S. Moretti, in preparation.